

Nacre-mimetic cerium-doped nano-hydroxyapatite/chitosan layered composite scaffolds regulate bone regeneration via OPG/RANKL signaling pathway

Xiao-Liang Liu

Shanghai Ninth People's Hospital, Shanghai Jiao Tong University School of Medicine

Chuan-Jian Zhang

Shanghai Normal University

Jing-Jing Shi

Shanghai Normal University

Qin-Fei Ke

Shanghai Normal University

Yu-Wei Ge

Shanghai Jiao Tong University Affiliated Shanghai Sixth People's Hospital

Zhen-An Zhu (✉ zhuzhenan2006@126.com)

Shanghai Ninth People's Hospital, Shanghai Jiao Tong University School of Medicine

Ya-Ping Guo

Shanghai Normal University

Research Article

Keywords: layered, nacre-mimetic, bone regeneration, Cerium, hydroxyapatite nanosheets

Posted Date: May 10th, 2022

DOI: <https://doi.org/10.21203/rs.3.rs-1612174/v1>

License:   This work is licensed under a Creative Commons Attribution 4.0 International License.

[Read Full License](#)

Additional Declarations: No competing interests reported.

Version of Record: A version of this preprint was published at Journal of Nanobiotechnology on August 8th, 2023. See the published version at <https://doi.org/10.1186/s12951-023-01988-y>.

Abstract

Background: There has been a major burden in diseases associated with critical bone defects. Despite many techniques for defect management has come into use, the common treatment remains controversial. Mollusk nacre is a natural structure with outstanding mechanical property due to its notable “brick-and-mortar” architecture. Combining inorganic brick with organic mortar, natural nacre displays remarkable tensile strength and fracture toughness. Rare elements have exhibited extraordinary promotive capacities in various aspects of physiological process. Cerium ions have been reported with prospective capacities in promoting bone regeneration in many studies. Herein, inspired by the nacre architecture, our team designed and fabricated a nacre-mimetic cerium-doped layered nano-hydroxyapatite/chitosan layered composite scaffold (CeHA/CS). The scaffold displayed a distinct layered HA/CS composite structure with intervals ranging from 50 to 200 μm , which provided compatible environments for the adhesion and proliferation of human bone marrow mesenchymal stem cells (hBMSCs), allowed the *in situ* growth of newly formed bone tissues. *In vitro*, The CeHA/CS layered composite scaffolds noticeably promoted the osteogenic process through the upregulated expressions of osteogenesis-related genes like RUNX2, and COL1 by the BMP-2/P-Smad1/5 signal pathway. And simultaneously, the layered scaffolds inhibited osteoclast differentiation evidenced by the reduced TRAP positive osteoclasts and lowered bone resorption. *In vivo*, calvarial defected rats revealed that the layered CeHA/CS scaffolds remarkably accelerated bone regeneration at the defect site and immunofluorescence suggested the layered CeHA/CS scaffolds lowered RANKL/OPG ratio. Our results showed that CeHA/CS scaffolds may become a promising platform for bone regeneration in critical defect management by promoting osteogenesis and inhibiting osteoclast activation.

1. Introduction

A bone defect is a common feature occurring in fractures and diseases that originated from infection, tumor, trauma and osteotomies which decreases bone mechanical strength and impairs bone biological function[1–3]. The natural regeneration mechanism of the body enables the healing of bone defects without medical intervention, especially in young patients[2, 4]. However, for patients with larger defects or attenuated bone self-regenerative function, surgical intervention is required[3, 5, 6]. Critical bone defects not only bring motor disability, but also cause economic impacts and wear long-term outcome for patients[7–9]. Although, there has been several clinical managements for bone defects, the ultimate treatment was still controversial[7, 10, 11]. One of the main concerns regarding repairing bone defects is to maintain mechanical strength to avoid secondary injury, which requires the bone architecture to be stable enough when bearing mechanical force[12, 13]. Besides, the bone needs a method to promote new bone formation at the defect site by promoting the proliferation of osteogenic tissues, materials involved in the treatment should be associated with bone formation process[14, 15].

In recent years, various bone scaffolds such as bioglass (BG), hydroxyapatite (HA), β -tricalcium phosphate (β -TCP) and chitosan (CS) have been proposed[2, 16–21]. With noticeable biocompatibility and osteoconductivity, those scaffolds have been widely used in attempts of building composite

bioscaffolds[22, 23]. Natural bone is a combination of organic-inorganic materials in which HA mineralized on collagen fibrils and it exhibits remarkable mechanical strength as well as natural nacre architecture[24, 25]. The preparation of natural high-performance structural materials such as nacre is highly promising for next-generation composites[26–29]. The nacre-inspired design is based on the formation of an ordered structure of hard-boosted platelets and soft polymers (natural mother-of-pearl contains 95 vol.% inorganic platelets)[30–33]. Natural nacre has excellent mechanical properties due to its special structure, which is attributed to platelet pullout, crack bridging and flexing mechanism[31–33]. Primarily, a bone repair material should be biocompatible with native tissues[34, 35]. CS is a natural cationic aminopolysaccharide and recognized with its biocompatibility in tissue engineering[36, 37]. However, single CS scaffold lacks the strength to bear weight force in critical bone defects[38]. Inspired by natural nacre, in our previous research, our team has created a nacre-mimetic layered HA/CS composite and validated its strength[39]. HA/CS scaffolds are recognized for their biodegradability and present excellent biocompatibility to biological tissues[40]. HA/CS scaffold can provide an appropriate environment for newly formed bone tissues, making it highly promising for bone tissue engineering.

Despite the nacre-mimetic HA/CS composite scaffold satisfies the strength requirement for bone tissue engineering. To promote bone regeneration, the materials involved should be promotive in bone formation. Although there are many chemicals which have been demonstrated playing significant roles in osteogenic process, like insulin-like growth factor-1 (IGF-1), transforming growth factor- β 1 (TGF- β 1), these chemicals are highly fragile when exposed outside the *vivo* environment and unstable when constructed into scaffold[41–43]. Alternatively, a small number of rare earth elements exist in the human body, such as lanthanum (La), cerium (Ce) and gadolinium (Gd), participating in stem cell differentiation and tissue regeneration[44]. Studies have shown that cerium deposition in the human bone is relatively high, indicating that bones may be the preferred precipitation sites for elemental cerium[45–47]. Cerium ions are associated with bone metabolism, inflammation toleration, antioxidation and antitumor[48–52]. Cerium ions have been studied for their anti-inflammatory effects in RA patients in which cerium particles acted as a ROS scavenger in the cellular environment to relieve the inflammatory level and reduce bone loss[50]. Besides, it's reported that as the ROS level reduces, processes of macrophages releasing inflammatory factors are abated, which is an essential pathway to activate inflammatory processes and promote bone resorption[51]. Previous studies have demonstrated that bio-scaffolds associated with cerium nanoparticles were able to inhibit RANKL-induced osteoclast differentiation to prevent bone resorption[53]. In addition, researchers also revealed the promotive capacity of Cerium element in osteogenic process, such as J. M. Li et al. found that ceria nanoparticles accelerated bone formation and enhanced endochondral ossification-based bone regeneration[49], and B. Lu et al. revealed that cerium oxide nanoparticles promoted osteoblast differentiation and proliferation through the ERK pathway[48].

In this study, we constructed the nacre-mimetic cerium-doped layered hydroxyapatite/chitosan (CeHA/CS) layered composite scaffolds and validated its potential for regulating osteogenic process and osteoclast differentiation *in vivo* and *in vitro*. we investigated the potential of CeHA/CS layered composite scaffolds for bone repair and regeneration, tested the biocompatibility of the scaffolds for hBMSCs *in vitro* and revealed osteogenic promotions on osteoblast differentiation by qPCR and western blot. The inhibitions

on RANK-induced osteoclast differentiation were also studied *in vitro*. Animal models were used to characterize their defect-repairing ability *in vivo*. The CeHA/CS layered composite scaffolds exhibited extraordinary potentials for bone regeneration.

2. Materials And Methods

2.1 Preparation of CeHA/CS layered scaffolds

CeHA/CS layered composite scaffolds were prepared as follows: First, 2 g CS was added to 50 ml 2% acetic acid and stirred for 3 h until CS was completely dissolved. After that, the bubbles were removed, and the solution was heated for 30 min, and the sonicated solution was poured into a 24-well plate and frozen in a refrigerator at -20°C . The frozen CS solution was placed in a freeze-dryer and dried for 72 h. The dried CS scaffolds were then immersed in a mixed solution containing 0.09 M CaCl_2 , 0.01 M $\text{Ce}(\text{NO}_3)_3 \cdot 6\text{H}_2\text{O}$ and 0.09 M Na_2CO_3 to deposit calcium carbonate on the CS scaffold. To form HA by mineralization, the composite was finally immersed in 0.02 M phosphate buffer solution (PBS) for 7 days to obtain CeHA/CS layered scaffolds.

2.2 Ion release testing of CeHA/CS layered scaffolds

0.4 g CeHA/CS layered scaffolds was added to 10 ml deionized water; then, an ion release experiment was performed in a constant temperature shaker at 37°C . At the corresponding time, 4 ml supernatant was taken out to measure its ion concentration by electron coupled plasma mass spectrometer, and then 4 ml deionized water was added to continue the experiment.

2.3 Characterization

The morphologies and layered structures of CS, HA/CS, CeHA/CS and were detected by scanning electron microscopy (SEM; JSM-6380LV, JEOL, Japan). X-ray diffractometer system (XRD, D/max-III C, Rigaku, Japan) was performed at an acceleration voltage of 40 kV in the range 5° – 60° (2θ). Fourier transform infrared (FTIR) spectroscopic analyzes (PerkinElmer, USA) were performed to detect functional groups in the range 4000 – 550 cm^{-1} .

2.4 Cell viability and adhesion

Cells were cultured with Dulbecco's modified eagle medium (DMEM) formulated with the addition of 10% fetal calf serum (FCS) and 1% penicillin/streptomycin at 37°C . The MC3T3-E1 cells (Shanghai Institutes for Biological Science, Chinese Academy of Science Shanghai, China) were seeded into a 96-well plate with a density of $1 \cdot 10^4$ cells per well. The media with an extraction solution of HA/CS and CeHA/CS were used to substitute DMEM after 24 h. Cell counting kit-8 (CCK-8, Dojindo, Kumamoto, Japan) was used to detect cell proliferation after cultivated for 1, 2 and 3 days. Human bone marrow mesenchymal stem cells (hBMSCs) (Shanghai Rochan Biotechnology CO. Shanghai, China) were seeded in a 24-well plate along with a scaffold for the observation of cell adhesion. Each well contained one scaffold with $1 \cdot 10^4$ cells and after 12-hour cultivation, cell-adhered scaffolds were washed with PBS and soaked in

2.5% glutaraldehyde for 20 minutes for fixation. Then, scaffolds were washed with PBS three times and progressively dehydrated using 75%, 85%, 95% and 100% ethanol. The morphologies of hBMSCs were characterized by SEM (Siri on 200, Fei, Hillsboro, USA).

2.5 Osteogenic capacity *in vitro*

hBMSCs were seeded in a 24-well plate at a density of $1 \cdot 10^4$ per well and cultivated for 7 days with osteogenesis differentiation medium, which was also the extraction solution of HA/CS and CeHA/CS. Then, hBMSCs were fixed with 4% paraformaldehyde and washed with PBS three times, followed with ALP staining (ALP kit Hongqiao, Shanghai, China) and optical microscopy. $4 \cdot 10^6$ hBMSCs were seeded in a 6-well plate per well with osteogenic differentiation media of extraction solution of HA/CS and CeHA/CS and cultivated for 7 days. A real-time quantitative polymerase chain reaction (RT-PCR, Applied Biosystems, Foster City, CA) was used to analyze the expression levels of osteogenic genes. The total RNA was collected with a RNeasy Mini kit (Qiagen: Valencia, CA, USA). The mRNA expressions of genes including collagen type I (COL-1), runt-related transcription factor 2 (RUNX2) and bone morphogenetic protein 2 (BMP-2) as well as a standard reference gene (GAPDH) were detected and analyzed by $2^{-\Delta\Delta Ct}$ method. The designed primers were as follows:

GAPDH forward 5'-CACCACCATGGAGAAGGCCG-3'

And reverse 5'-ATGATGTTCTGGGCAGCCCC-3'

RUNX2 forward 5'-GACTGTGGTTACCGTCATGGC-3'

And reverse 5'-ACTTGGTTTTTCATAACAGCGGA-3'

COL-1 forward 5'- GAGGGCCAAGACGAAGACATC – 3'

And reverse 5'- CAGATCACGTCATCGCACAAC – 3'

BMP2 forward 5'- GGAACGGACATTCGGTCCTT – 3'

And reverse 5'- CACCATGGTCGACCTTTAGGA – 3'

The osteoblast-associated proteins of BMP-2, RUNX-2, COL1 and P-Smad1/5 were characterized by the western blot method. hBMSCs were cultivated in a media of DMEM and extraction solution of HA/CS and CeHA/CS for three days. Then, radioimmunoprecipitation assay (RIPA) lysis buffer solution was used to soak cells for 20 minutes, and the lysed samples were collected in 1.5-ml microcentrifuge tubes. Samples were centrifuged at 12,000 rpm for 10 minutes, and supernatants were collected. Bicinchoninic acid assay (BCA) was used to detect the concentration of supernatants. Detected samples were loaded in SDS-PAGE gel for electrophoresis and transferred to polyvinylidene difluoride (PVDF) membranes. After blocking in 5% milk for 1 h, the membranes were incubated with primary antibodies at room temperature for 4 h and then washed by TBST three times. These membranes were incubated with secondary

antibodies (Cell Signaling Technology, Shanghai, China) for 1 h. Finally, blotting results were checked by the Odyssey infrared imaging system (LI-COR Biosciences, Lincoln, NE).

2.6 Inhibition of osteoclast differentiation *in vitro*

Bone marrow macrophages (BMMs) were flushed out from the tibiae and femurs of 4–6-week-old c57BL/6 mice (16–18 g) bought from the Animal Centre Research Committee of the Shanghai Ninth People's Hospital (Shanghai, China). Cells were collected and cultured in α -MEM (Gibco; Thermo Fisher Scientific, Inc., Waltham, MA, USA) with 30 ng/ml M-CSF (R&D Systems, Inc., Minneapolis, MN, USA), 10% FBS and 1% penicillin-streptomycin at 37 °C. Media were changed every 3 days. After 7 days, cells were dissociated and reseeded in the plates of each experimental group, and 30 ng/ml M-CSF and 50 ng/ml RANKL (R&D Systems, Inc., Minneapolis, MN, USA) were used as media to stimulate osteoclast differentiation. After 7 days, cells were fixed with 4% paraformaldehyde and washed three times by PBS. Osteoclastic differentiation was observed by TRAP staining (Sigma Aldrich, Merck KGaA). The radiographs of TRAP-positive areas were reserved using Image-Pro Plus 6.0 (Media Cybernetics, Inc., Rockville, MD, USA). For f-actin analysis, cells were fixed with 4% paraformaldehyde and permeabilized with 0.1% (v/v) Triton-100 (Sigma Aldrich, Merck KGaA) and then stained with rhodamine-conjugated phalloidin (Cytoskeleton, Inc., Denver, CO, USA) at 37 °C for 1 h. F-actin rings were characterized by LSM5 confocal microscope (magnification: 10x; Carl Zeiss AG, Oberkochen, Germany).

2.7 Animal experiments

15 Sprague-Dawley (SD) female rats (200–250 g, 6/group) were bought from Shanghai Experiment Animal Research Centre, and all experimental procedures were approved by the Animal's Hospital of Shanghai Jiao Tong University. After injected intraperitoneally with sodium pentobarbital for anesthesia, SD rats were shaved overhead, and 5-mm diameter holes were drilled on the skull to create a bilateral critical-size calvarial-defect model. the scaffolds of HA/CS and CeHA/CS were then filled into the drilled space before the scalps were sutured. All rats were sacrificed after 12 weeks, and the calvaria skull caps were dissected and soaked in 4% phosphate-buffered formalin solution for 7 days. Then, micro-CT was performed using a micro-CT system (mCT-80, Scanco Medical AG, Switzerland) on soaked samples with parameters of a voltage of 90 kV, current of 88 uA and voxel size of 28 μ m. 3d reconstruction was made by the micro-CT images. Bone mineral density (BMD) and new bone volume/tissue volume (BV/TV) values were analyzed as well. 3 and 21 days before the rats were sacrificed, fluorescent-labeled alizarin red (30 mg/kg, Sigma Aldrich) and calcein (30 mg/kg, Sigma Aldrich) had been injected into each rat. Labeled rats' skulls were cut into 150-nm-thick slices by a microtome (Leica, Hamburg, Germany) and analyzed by confocal laser scanning microscope (Leica, Heidelberg, Germany, Alizarin red: 543/580–670 nm, calcein: 488/500–550 nm). The PC-based analysis system was used to quantify the mineralization rate (MAR). For morphologic observation, cranium samples were impeded in paraffin and stained with Masson's trichrome.

3. Results

3.1 Morphology of CeHA/CS layered scaffolds

The CS layered scaffold was prepared by stirring the CS slurry evenly, followed by freeze-drying technology (Figs. 1a and 1b). The high-resolution SEM image (Fig. 1b) indicates that the CS layer has a smooth surface. The EDS spectrum shows that CS mainly contains C and O elements. CS is a semi-crystalline organic matrix, which is confirmed by the peaks at $2\theta = 20^\circ$ and 28° in the XRD pattern (Fig. 2c). The FTIR spectrum of the CS layered scaffold also shows the characteristic vibration peaks of CS at 3400 cm^{-1} caused by the OH- tensile vibration, and the band at 1648 cm^{-1} corresponds to the amide I vibration, amino N-H deformation and oscillating vibration. The absorption peaks appear at 1595 and 895 cm^{-1} , while the absorption peaks at 1420 cm^{-1} can be attributed to the vibration of C-N in the main group, the vibration at 1030 and 1066 cm^{-1} to the tensile vibration of C-O, and the peak at 1150 cm^{-1} to the tensile vibration of C-O-C group (Figure. 2d) [54].

Because a large amount of PO_4^{3-} is contained in PBS and the dissolution constant of HA is greater than CaCO_3 , CaCO_3 will be converted to HA *in situ* in PBS. Therefore, we can immerse the CaCO_3 /CS layered composite in PBS so that CaCO_3 attached to the layer can be converted into HA *in situ*. After doping with rare earth elements, the morphology of CeHA/CS layered scaffolds did not change, preserving a well-layered structure (Figs. 1g). High-resolution SEM images show that the HA converted by CaCO_3 shows a flaky structure (Figs. 1e and 1h). The EDS chart shows that CeHA/CS layered scaffolds detected Ce elements compared to HA/CS. This indicates that rare earth elements have been successfully added to HA/CS scaffolds.

The transformed HA matched well with JCPDS card no. 09-0432 (Fig. 1i). By comparing the XRD (Fig. 2c) and FTIR (Fig. 2d) plots of HA/CS and CeHA/CS layered composites, the positions of the peaks and vibration peaks have not changed, indicating that the addition of rare earth elements will not change the scaffold crystal structure and composition. The FTIR plots of HA/CS and CeHA/CS layered composite show that the vibration of PO_4^{3-} appears at 603 cm^{-1} (ν_4), 960 cm^{-1} (ν_1), 1025 cm^{-1} (ν_3), 1648 cm^{-1} . And 1420 cm^{-1} can be attributed to the amide I vibration and the vibration in the primary amide group of CS respectively[54, 55]. Interestingly, the vibrational fractions of CO_3^{2-} were detected in the FTIR of HA/CS and CeHA/CS layered composite at 1475 cm^{-1} and 875 cm^{-1} , respectively. This is because HA is converted from CaCO_3 , while CO_3^{2-} may be partially retained in the crystal lattice of HA.

3.2 Ion release and compression properties of CeHA/CS layered scaffolds

The release characteristics of the various ions of CeHA/CS layered composite were studied by the ICP technique (Figs. 2e and 2f). After immersing the composite in ultrapure water, Ca^{2+} and Ce^{3+} ions were rapidly released and then tended to gentle. After 144 h, the cumulative release of Ca^{2+} ions were $260.82\text{ }\mu\text{M}$, and the cumulative release of Ce^{3+} ions was $0.36\text{ }\mu\text{M}$. The release of the rare earth ions was within a safe concentration. The compression performance of all composites suddenly changed in 2 mm because

it is initially caused by the compression of HA, which is a brittle material (Figure. 2g). The compression performance after 2 mm was improved due to the compression of CS as it is a plastic material.

3.3 Cytotoxicity and adhesion of CeHA/CS scaffolds

The MC3T3-E1 cells were cultured in 96-well plates at a density of $1 \cdot 10^4$ cells per well with an extraction solution of HA/CS and CeHA/CS for 1, 2 and 3 days and then tested for viability by CCK-8 kit. In the curve, cell numbers were continuously increased with time (Fig. 3a), and the number of cells nearly tripled after 96 h compared to that at 24 h. Intergroup curves have no distinct differences, indicating that these scaffolds did not attenuate MC3T3-E1 cell proliferation (Fig. 3a). The hBMSCs were seeded onto scaffolds and observed by SEM. The results showed hBMSCs adhered to the surface of scaffolds with protruded filopodia, and similar adhesions were found in each group; thus, scaffolds provided a suitable condition for cell-adhering capacity (Fig. 3b).

3.4 Osteogenic promotion of CeHA/CS scaffolds *in vitro*

ALP staining was used to analyze the osteogenic effects of the scaffolds. After cultivated with scaffolds and osteogenic differentiative solution for 7 days, the CeHA/CS scaffolds gained the highest ALP activity in comparison with HA/CS and control (Fig. 3c and 3e). Similar results were seen in alizarin red staining in which cells were cultivated with scaffolds for 20 days, the HA/CS and CeHA/CS scaffolds gained better alizarin activity than control, and the CeHA/CS scaffolds promoted the highest activity (Fig. 3d and 3f). Furthermore, the osteogenic capacity of scaffolds was investigated by RT-PCR, and the results revealed that HA/CS scaffolds doped with cerium promoted the expression of BMP-2, COL1 and RUNX2 compared with control group (Fig. 4f to 4h). The osteogenic capacity was also validated by western blot analysis. CeHA/CS scaffolds presented the highest expression of BMP-2, COL1, RUNX2, P-Smad1/5 genes (Fig. 4a to 4e), which demonstrated osteogenesis-associated genes expressions were promoted.

3.5 BMM differentiation inhibition of CeHA/CS scaffolds *in vitro*

Cells in the control group and HA/CS scaffold obtained the highest TRAP activity but in the CeHA/CS scaffolds groups, it was relatively lower (Fig. 5a to 5c). Thus, the CeHA/CS scaffolds reduced osteoclast differentiation. However, HA/CS scaffolds didn't affect the TRAP activity compared with control. CeHA/CS scaffolds also gained fewer f-actin rings compared with control and HA/CS scaffolds (Fig. 5d and 5f), which revealed the inhibitions on bone resorption activity. Generally, bone resorption process would be activated when pre-osteoclasts were differentiated into mature osteoclasts and induce bone loss. However, BMM cultivated with the CeHA/CS scaffolds were keep inactivated towards bone slices and the surfaces in CeHA/CS scaffolds group were obviously smooth (Fig. 5f). These results indicate that CeHA/CS scaffolds have inhibited osteoclast differentiation.

3.6 *In vivo* rat calvarial defect models

The micro-CT images of calvarium revealed that rats with CeHA/CS scaffolds generated the most volume of newly formed bone compared with rats with control and HA/CS scaffolds (Fig. 6a). The same was observed for BMD: the BMDs in the CeHA/CS scaffolds were much higher than those in the other two groups (Fig. 6b). Also, the BV/TV values were higher in the CeHA/CS scaffolds, indicating CeHA/CS scaffolds remarkably contributed to the new bone formation *in vivo* (Fig. 6c). Fluorochromes marks indicated the growth in 18 days and rats with CeHA/CS scaffolds obtained the best growth rate (Fig. 6d and 6e).

Histomorphology observations were made 3 months after calvarium defects were implanted with scaffolds by H&E staining. From the sagittal plane of the defects, it was observed that CeHA/CS scaffolds were accelerated in new bone formation inside the defects (Fig. 7a). Moreover, the influences of scaffolds on osteoclasts were analyzed by immunofluorescence labeling. The RANKL/OPG ratio was reduced in the CeHA/CS scaffolds in comparison with control and HA/CS scaffolds (Fig. 7b), which demonstrated the CeHA/CS scaffolds reconstruct bone tissue by promoting osteogenic activities and attenuated osteoclast differentiation.

4. Discussion

Large bone defects have always been a major challenge in orthopedic procedures[1–3], and with damaged physical stability and impaired biofunction, defected bones are easy to cause fractures and difficult to perform surgical procedures[5, 6]. Various types of scaffolds have been studied for healing large bone defects, and scaffolds that promote new bone formation have been regarded as a prospective strategy[2, 3, 16–21].

Herein we created a scaffold with the strength of releasing osteogenesis-related elements to explore the possibilities of promoting bone regeneration. The CeHA/CS layered composite scaffolds were firstly prepared by dissolving CS into acetic acid, and after stirring and heating, the mixed solution was frozen and dried to form solid CS scaffolds. Then, dried CS scaffolds were immersed into the solutions of CaCl_2 , $\text{Ce}(\text{NO}_3)_3 \cdot 6\text{H}_2\text{O}$ and Na_2CO_3 , and calcium carbonate was generated on the CS scaffold doped with cerium. Fabricated scaffolds were then deposited with HA mineralization by immersing with PBS. Ultimately, the CeHA/CS layered composite scaffolds were successfully produced. SEM showed the scaffolds of CeHA/CS were arranged as layered structures (Fig. 1g), which shows that the addition of rare elements does not affect the original structure. The layered structures provided appropriate sites for osteoblast cells to contact and adhere (Fig. 3b). HA/CS scaffolds are biocompatible with living tissues, and no toxic effects were observed in this research (Fig. 3a). The layered structure provided an applicable bridge for cell migration and proliferation. CCK-8 results suggested that the CeHA/CS layered scaffolds have no toxic effects on MC3T3-E1 cells proliferation (Fig. 3a), and the SEM results indicate hBMSCs were stretched on the sheet-like surface and maintained steadily, adhering to the scaffolds (Fig. 3b). In the animal model, the sagittal plane of the defects displayed substantial penetrated connective tissues and newly formed bone structures (Fig. 7a), indicating the layered scaffolds provide excellent space for tissue growth in scaffolds. Penetrated tissues adhered to the scaffolds and proliferated (Fig. 7a),

contributing to the growth of regenerated bones. Our work demonstrated that the regenerated bone tissues could prospectively adapt to our layered scaffolds.

Cerium is known as a rare element with significant positive functions, especially in the bone formation process[44]. It was reported that cerium can upregulate osteogenic gene expression and accelerate new bone formation[48, 49]. Herein, we generated the CeHA/CS scaffolds by incorporating cerium ions into the CeHA/CS scaffolds. In this way, cerium elements were within the CeHA/CS scaffolds, and meanwhile, the basic layered structure was preserved. We tested the CeHA/CS scaffolds' osteogenic capacities and compared them with the previous scaffolds. It was shown that with cerium added to the HA/CS scaffolds, there was an obvious increase in ALP staining activity (Fig. 3c and 3e), indicating that CeHA/CS scaffolds significantly promoted the osteogenic activity. Similar results were observed in the alizarin red analysis. After 20 days of cultivation, the CeHA/CS scaffolds gained higher alizarin red activity (Fig. 3d and 3f), indicating improved calcium deposition. The results showed that the HA/CS and CeHA/CS scaffolds had excellent performances on ALP and alizarin red staining, while the CeHA/CS scaffolds performed better than the primary HA/CS scaffolds. Further, we studied the mechanism of osteogenic promotion in the presence of cerium by RT-PCR and western blot techniques. The expressions of osteogenic-associated genes of RUNX2, COL1, BMP-2 and P-Smad1/5 significantly improved in the group cultivated with CeHA/CS scaffolds compared to the control and HA/CS scaffolds in western blots (Fig. 4a to 4e). The RT-PCR results revealed the same trend in the osteogenic mechanism as it upregulated the expressions of RUNX-2, BMP-2, COL1, indicating the osteogenic pathway was activated (Fig. 4f to 4h). In the animal experiment, micro-CT showed the bone defects in the CeHA/CS group were better healed (Fig. 6a to 6c), and H&E staining indicated connective tissues and newly formed bones penetrated between layered structures (Fig. 7a).

In terms of bone resorption, cerium was known for acting as an ROS scavenger in the cellular environment[50, 52, 53, 56]. ROS in the cellular environment can lead to inflammation in tissues and may introduce osteoclast differentiation[51]. And cerium ions were proven to act as an anti-inflammation factor in macrophage polarization, which may inhibit pro-inflammation macrophage differentiation and eventually inhibited the osteoclast differentiation[50, 53]. In our study, CeHA/CS scaffolds attenuated the differentiation of BMMs into osteoclasts with downregulated TRAP activities (Fig. 5a) and successfully reduced bone resorption activity on the surface of bone slices (Fig. 5f). Also, in calvarial-defect rats, immunofluorescence histochemistry staining displayed a reduced RANKL/OPG ratio in the rats with CeHA/CS scaffolds implanted (Fig. 7b). The CeHA/CS scaffolds significantly accelerated new bone formation via osteogenic promotion and osteoclastic inhibition.

5. Conclusion

The layered composite scaffolds were constructed by a freeze-dry strategy with $\text{Ce}(\text{NO}_3)_3 \cdot 6\text{H}_2\text{O}$ dispersed in the compound solution. The CeHA/CS scaffolds provided an appropriate environment for cell proliferation and were characterized for their osteogenic functions owing to the upregulation of RUNX, BMP-2, COL1 and P-Smad1/5 in hBMSCs. In addition, the CeHA/CS scaffolds inhibited osteoclast

differentiation with fewer TRAP positive cells and attenuated bone resorption activities. Results *in vivo* revealed the promotive effects on new bone formation and mineralization in a rat calvarial defect model, and reduced RANKL/OPG ratio was observed as well. The CeHA/CS scaffolds exhibit remarkable potential for bone healing and regeneration.

Authors' contributions

CJZ, XLL and JJS initiated the study, designed the experiments and wrote the paper. YWG and QFK performed the experiments and statistical analyses. ZAZ and YPG helped with animal experiments. All authors read and approved the final manuscript.

Declarations

Authors' contributions

CJZ, XLL and JJS initiated the study, designed the experiments and wrote the paper. YWG and QFK performed the experiments and statistical analyses. ZAZ and YPG helped with animal experiments. All authors read and approved the final manuscript.

Funding

This research was supported by National Natural Science Foundation of China (No. 82002270, No. 81572158).

Availability of data and materials

The data that support the findings of this study are available from the corresponding author upon reasonable request.

Ethics approval and consent to participate

All experimental procedures were approved by the Institutional Animal Care and Use Committee (IACUC) of the Shanghai Ninth People's Hospital, Shanghai Jiao Tong University School of Medicine. All mice were provided by the Research Council of the Animal Center of the Shanghai Ninth People's Hospital (China). Consent for publication All authors agree to publish this manuscript.

Competing interests

The authors declare no competing financial interest

References

1. G. Fernandez de Grado, L. Keller, Y. Idoux-Gillet, Q. Wagner, A. M. Musset, N. Benkirane-Jessel, et al. Bone substitutes: a review of their characteristics, clinical use, and perspectives for large bone

- defects management. *Journal of tissue engineering*. 2018; 9: 2041731418776819.
2. A. A. El-Rashidy, J. A. Roether, L. Harhaus, U. KneserA. R. Boccaccini. Regenerating bone with bioactive glass scaffolds: A review of in vivo studies in bone defect models. *Acta Biomater*. 2017; 62: 1–28.
 3. H. Lu, Y. Liu, J. Guo, H. Wu, J. WangG. Wu. Biomaterials with Antibacterial and Osteoinductive Properties to Repair Infected Bone Defects. *Int J Mol Sci*. 2016; 17(3): 334.
 4. B. Safari, S. DavaranA. Aghanejad. Osteogenic potential of the growth factors and bioactive molecules in bone regeneration. *Int J Biol Macromol*. 2021; 175: 544–557.
 5. P. ToogoodT. Miclau. Critical-Sized Bone Defects: Sequence and Planning. *Journal of orthopaedic trauma*. 2017; 31 Suppl 5: S23-S26.
 6. H. Bezstarosti, W. J. Metsemakers, E. M. M. van Lieshout, L. W. Voskamp, K. Kortram, M. A. McNally, et al. Management of critical-sized bone defects in the treatment of fracture-related infection: a systematic review and pooled analysis. *Arch Orthop Trauma Surg*. 2021; 141(7): 1215–1230.
 7. A. Nauth, E. Schemitsch, B. Norris, Z. NollinJ. T. Watson. Critical-Size Bone Defects: Is There a Consensus for Diagnosis and Treatment? *Journal of orthopaedic trauma*. 2018; 32 Suppl 1: S7-S11.
 8. C. Mauffrey, B. T. BarlowW. Smith. Management of segmental bone defects. *The Journal of the American Academy of Orthopaedic Surgeons*. 2015; 23(3): 143–153.
 9. G. B. D. F. Collaborators. Global, regional, and national burden of bone fractures in 204 countries and territories, 1990–2019: a systematic analysis from the Global Burden of Disease Study 2019. *Lancet Healthy Longev*. 2021; 2(9): e580-e592.
 10. A. StahlY. P. Yang. Regenerative Approaches for the Treatment of Large Bone Defects. *Tissue Eng Part B Rev*. 2021; 27(6): 539–547.
 11. J. C. AureganT. Begue. Induced membrane for treatment of critical sized bone defect: a review of experimental and clinical experiences. *Int Orthop*. 2014; 38(9): 1971–1978.
 12. S. H. Lee, K. G. Lee, J. H. Hwang, Y. S. Cho, K. S. Lee, H. J. Jeong, et al. Evaluation of mechanical strength and bone regeneration ability of 3D printed kagome-structure scaffold using rabbit calvarial defect model. *Materials science & engineering. C, Materials for biological applications*. 2019; 98: 949–959.
 13. S. G. Hopp, L. E. DahnersJ. A. Gilbert. A study of the mechanical strength of long bone defects treated with various bone autograft substitutes: an experimental investigation in the rabbit. *J Orthop Res*. 1989; 7(4): 579–584.
 14. A. R. Amini, C. T. LaurencinS. P. Nukavarapu. Bone tissue engineering: recent advances and challenges. *Critical reviews in biomedical engineering*. 2012; 40(5): 363–408.
 15. R. Dimitriou, E. Jones, D. McGonagleP. V. Giannoudis. Bone regeneration: current concepts and future directions. *BMC Med*. 2011; 9: 66.
 16. A. Szczes, L. HolyszE. Chibowski. Synthesis of hydroxyapatite for biomedical applications. *Advances in colloid and interface science*. 2017; 249: 321–330.

17. M. Bohner, B. L. G. SantoniN. Dobelin. beta-tricalcium phosphate for bone substitution: Synthesis and properties. *Acta Biomater.* 2020; 113: 23–41.
18. R. LogithKumar, A. KeshavNarayan, S. Dhivya, A. Chawla, S. SaravananN. Selvamurugan. A review of chitosan and its derivatives in bone tissue engineering. *Carbohydrate polymers.* 2016; 151: 172–188.
19. Y. Zhu, L. Kong, F. Farhadi, W. Xia, J. Chang, Y. He, et al. An injectable continuous stratified structurally and functionally biomimetic construct for enhancing osteochondral regeneration. *Biomaterials.* 2019; 192: 149–158.
20. W. Chen, X. Shen, Y. Hu, K. Xu, Q. Ran, Y. Yu, et al. Surface functionalization of titanium implants with chitosan-catechol conjugate for suppression of ROS-induced cells damage and improvement of osteogenesis. *Biomaterials.* 2017; 114: 82–96.
21. H. Zhao, C. Wu, D. Gao, S. Chen, Y. Zhu, J. Sun, et al. Antitumor Effect by Hydroxyapatite Nanospheres: Activation of Mitochondria-Dependent Apoptosis and Negative Regulation of Phosphatidylinositol-3-Kinase/Protein Kinase B Pathway. *ACS nano.* 2018; 12(8): 7838–7854.
22. L. Roseti, V. Parisi, M. Petretta, C. Cavallo, G. Desando, I. Bartolotti, et al. Scaffolds for Bone Tissue Engineering: State of the art and new perspectives. *Materials science & engineering. C, Materials for biological applications.* 2017; 78: 1246–1262.
23. S. Yin, W. Zhang, Z. ZhangX. Jiang. Recent Advances in Scaffold Design and Material for Vascularized Tissue-Engineered Bone Regeneration. *Advanced healthcare materials.* 2019; 8(10): e1801433.
24. A. K. Nair, A. Gautieri, S. W. ChangM. J. Buehler. Molecular mechanics of mineralized collagen fibrils in bone. *Nat Commun.* 2013; 4: 1724.
25. A. K. Nair, A. GautieriM. J. Buehler. Role of intrafibrillar collagen mineralization in defining the compressive properties of nascent bone. *Biomacromolecules.* 2014; 15(7): 2494–2500.
26. J. Y. Woo, J. H. Oh, S. JoC. S. Han. Nacre-Mimetic Graphene Oxide/Cross-Linking Agent Composite Films with Superior Mechanical Properties. *ACS nano.* 2019; 13(4): 4522–4529.
27. Y. Choi, D. Jeon, Y. Choi, D. Kim, N. Kim, M. Gu, et al. Interface Engineering of Hematite with Nacre-like Catalytic Multilayers for Solar Water Oxidation. *ACS nano.* 2019; 13(1): 467–475.
28. X. Shi, H. Wang, X. Xie, Q. Xue, J. Zhang, S. Kang, et al. Bioinspired Ultrasensitive and Stretchable MXene-Based Strain Sensor via Nacre-Mimetic Microscale "Brick-and-Mortar" Architecture. *ACS nano.* 2019; 13(1): 649–659.
29. Y. Zhang, J. Tian, J. ZhongX. Shi. Thin Nacre-Biomimetic Coating with Super-Anticorrosion Performance. *ACS nano.* 2018; 12(10): 10189–10200.
30. A. Eckert, T. Rudolph, J. Guo, T. MangA. Walther. Exceptionally Ductile and Tough Biomimetic Artificial Nacre with Gas Barrier Function. *Advanced materials (Deerfield Beach, Fla.).* 2018; 30(32): e1802477.
31. T. Li, B. Ma, J. Xue, D. Zhai, P. Zhao, J. Chang, et al. Bioinspired Biomaterials with a Brick-and-Mortar Microstructure Combining Mechanical and Biological Performance. *Advanced healthcare materials.* 2020; 9(4): e1901211.

32. J. H. E. Cartwright, A. G. ChecaC. I. Sainz-Diaz. Nacre Is a Liquid-Crystal Thermometer of the Oceans. *ACS nano*. 2020; 14(8): 9277–9281.
33. J. Wang, Q. ChengZ. Tang. Layered nanocomposites inspired by the structure and mechanical properties of nacre. *Chem Soc Rev*. 2012; 41(3): 1111–1129.
34. H. D. Kim, S. Amirthalingam, S. L. Kim, S. S. Lee, J. RangasamyN. S. Hwang. Biomimetic Materials and Fabrication Approaches for Bone Tissue Engineering. *Advanced healthcare materials*. 2017; 6(23):
35. D. Lopes, C. Martins-Cruz, M. B. OliveiraJ. F. Mano. Bone physiology as inspiration for tissue regenerative therapies. *Biomaterials*. 2018; 185: 240–275.
36. A. Muxika, A. Etxabide, J. Uranga, P. GuerreroK. de la Caba. Chitosan as a bioactive polymer: Processing, properties and applications. *Int J Biol Macromol*. 2017; 105(Pt 2): 1358–1368.
37. Z. K. Cui, S. Kim, J. J. Baljon, B. M. Wu, T. AghalooM. Lee. Microporous methacrylated glycol chitosan-montmorillonite nanocomposite hydrogel for bone tissue engineering. *Nat Commun*. 2019; 10(1): 3523.
38. M. Zhang, T. Wan, P. Fan, K. Shi, X. Chen, H. Yang, et al. Photopolymerizable chitosan hydrogels with improved strength and 3D printability. *Int J Biol Macromol*. 2021; 193(Pt A): 109–116.
39. C. J. Zhang, M. Hu, Q. F. Ke, C. X. Guo, Y. J. GuoY. P. Guo. Nacre-inspired hydroxyapatite/chitosan layered composites effectively remove lead ions in continuous-flow wastewater. *Journal of hazardous materials*. 2020; 386: 121999.
40. S. Banerjee, B. Bagchi, S. Bhandary, A. Kool, N. A. Hoque, P. Biswas, et al. Antimicrobial and biocompatible fluorescent hydroxyapatite-chitosan nanocomposite films for biomedical applications. *Colloids Surf B Biointerfaces*. 2018; 171: 300–307.
41. J. Yan, J. W. Herzog, K. Tsang, C. A. Brennan, M. A. Bower, W. S. Garrett, et al. Gut microbiota induce IGF-1 and promote bone formation and growth. *Proc Natl Acad Sci U S A*. 2016; 113(47): E7554-E7563.
42. Y. Tang, M. Hu, Y. Xu, F. Chen, S. Chen, M. Chen, et al. Megakaryocytes promote bone formation through coupling osteogenesis with angiogenesis by secreting TGF-beta1. *Theranostics*. 2020; 10(5): 2229–2242.
43. L. F. BonewaldG. R. Mundy. Role of transforming growth factor-beta in bone remodeling. *Clin Orthop Relat Res*. 1990; (250): 261–276.
44. S. Zaichick, V. Zaichick, V. KarandashevS. Nosenko. Accumulation of rare earth elements in human bone within the lifespan. *Metallomics: integrated biometal science*. 2011; 3(2): 186–194.
45. X. FangH. Song. Synthesis of cerium oxide nanoparticles loaded on chitosan for enhanced auto-catalytic regenerative ability and biocompatibility for the spinal cord injury repair. *Journal of photochemistry and photobiology. B, Biology*. 2019; 191: 83–87.
46. A. Marino, C. Tonda-Turo, D. De Pasquale, F. Ruini, G. Genchi, S. Nitti, et al. Gelatin/nanoceria nanocomposite fibers as antioxidant scaffolds for neuronal regeneration. *Biochimica et biophysica acta. General subjects*. 2017; 1861(2): 386–395.

47. P.-P. Zhao, H.-R. Hu, J.-Y. Liu, Q.-F. Ke, X.-Y. Peng, H. Ding, et al. Gadolinium phosphate/chitosan scaffolds promote new bone regeneration via Smad/Runx2 pathway. *Chemical Engineering Journal*. 2019; 359: 1120–1129.
48. B. Lu, D. Y. Zhu, J. H. Yin, H. Xu, C. Q. Zhang, Q. F. Ke, et al. Incorporation of cerium oxide in hollow mesoporous bioglass scaffolds for enhanced bone regeneration by activating the ERK signaling pathway. *Biofabrication*. 2019; 11(2): 025012.
49. J. Li, F. Kang, X. Gong, Y. Bai, J. Dai, C. Zhao, et al. Ceria nanoparticles enhance endochondral ossification-based critical-sized bone defect regeneration by promoting the hypertrophic differentiation of BMSCs via DHX15 activation. *FASEB journal: official publication of the Federation of American Societies for Experimental Biology*. 2019; 33(5): 6378–6389.
50. J. Kim, H. Y. Kim, S. Y. Song, S. H. Go, H. S. Sohn, S. Baik, et al. Synergistic Oxygen Generation and Reactive Oxygen Species Scavenging by Manganese Ferrite/Ceria Co-decorated Nanoparticles for Rheumatoid Arthritis Treatment. *ACS nano*. 2019; 13(3): 3206–3217.
51. F. Zeng, Y. Wu, X. Li, X. Ge, Q. Guo, X. Lou, et al. Custom-Made Ceria Nanoparticles Show a Neuroprotective Effect by Modulating Phenotypic Polarization of the Microglia. *Angewandte Chemie (International ed. in English)*. 2018; 57(20): 5808–5812.
52. I. Celardo, J. Z. Pedersen, E. TraversaL. Ghibelli. Pharmacological potential of cerium oxide nanoparticles. *Nanoscale*. 2011; 3(4): 1411–1420.
53. K. Yuan, J. Mei, D. Shao, F. Zhou, H. Qiao, Y. Liang, et al. Cerium Oxide Nanoparticles Regulate Osteoclast Differentiation Bidirectionally by Modulating the Cellular Production of Reactive Oxygen Species. *International journal of nanomedicine*. 2020; 15: 6355–6372.
54. S. Turk, I. Altinsoy, G. Celebi Efe, M. Ipek, M. OzacarC. Bindal. 3D porous collagen/functionalized multiwalled carbon nanotube/chitosan/hydroxyapatite composite scaffolds for bone tissue engineering. *Materials science & engineering. C, Materials for biological applications*. 2018; 92: 757–768.
55. M. Li, Y. Wang, Q. Liu, Q. Li, Y. Cheng, Y. Zheng, et al. In situ synthesis and biocompatibility of nano hydroxyapatite on pristine and chitosan functionalized graphene oxide. *Journal of materials chemistry. B*. 2013; 1(4): 475–484.
56. S. M. Hirst, A. S. Karakoti, R. D. Tyler, N. Sriranganathan, S. SealC. M. Reilly. Anti-inflammatory properties of cerium oxide nanoparticles. *Small (Weinheim an der Bergstrasse, Germany)*. 2009; 5(24): 2848–2856.

Figures

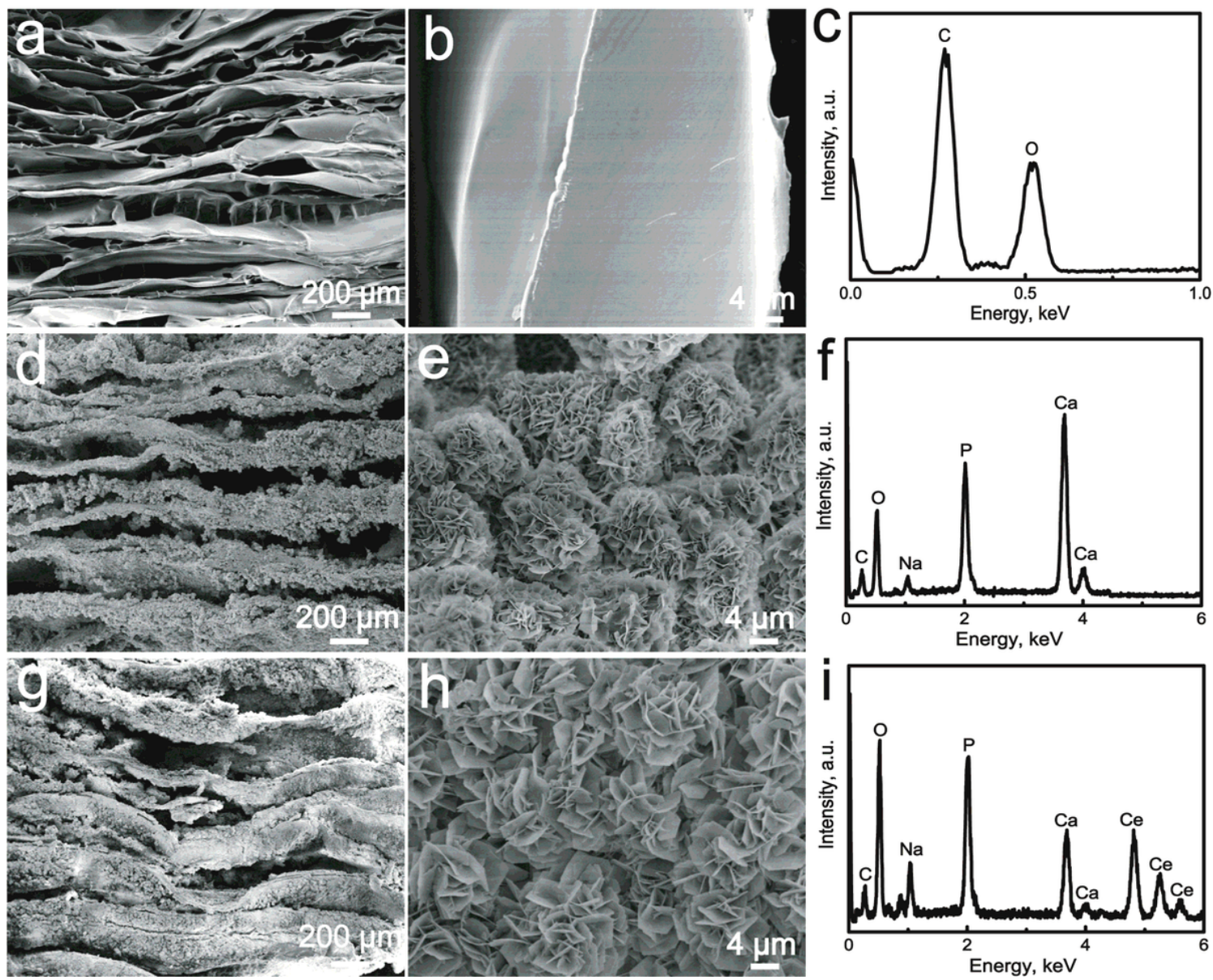


Figure 1

(a, b) SEM images of CS scaffold; (d, e) SEM images of HA/CS scaffold; (g, h) SEM images of CeHA/CS scaffold; (c, f, i) EDS spectrum.

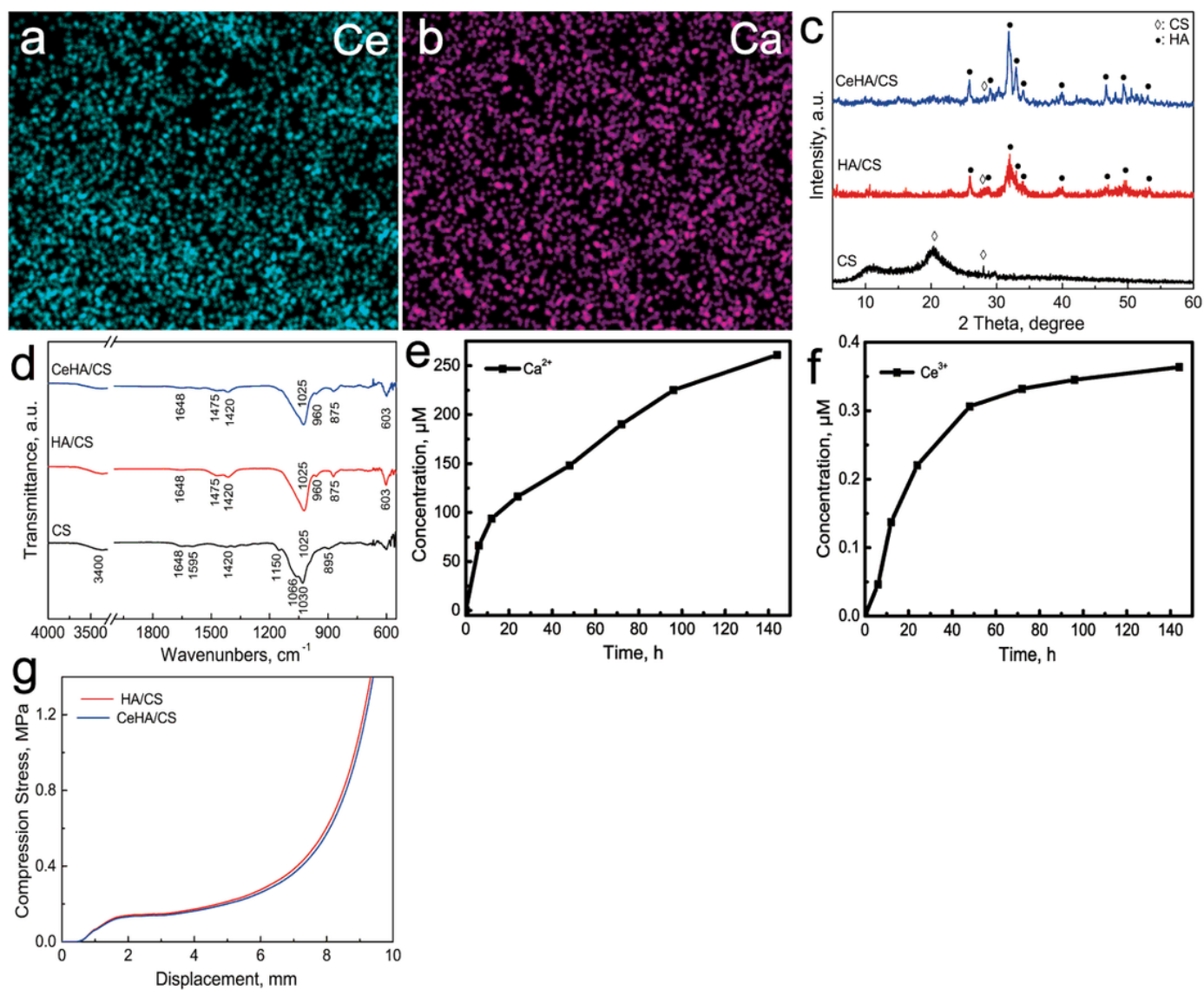


Figure 2

(a, b) Ce, Ca element distribution image respectively; (c) XRD and (d) FTIR spectra of CS, HA/CS, CeHA/CS; (e, f) Ion release curves of Ca²⁺ and Ce³⁺ for CeHA/CS respectively; (g) Composite compression performance.

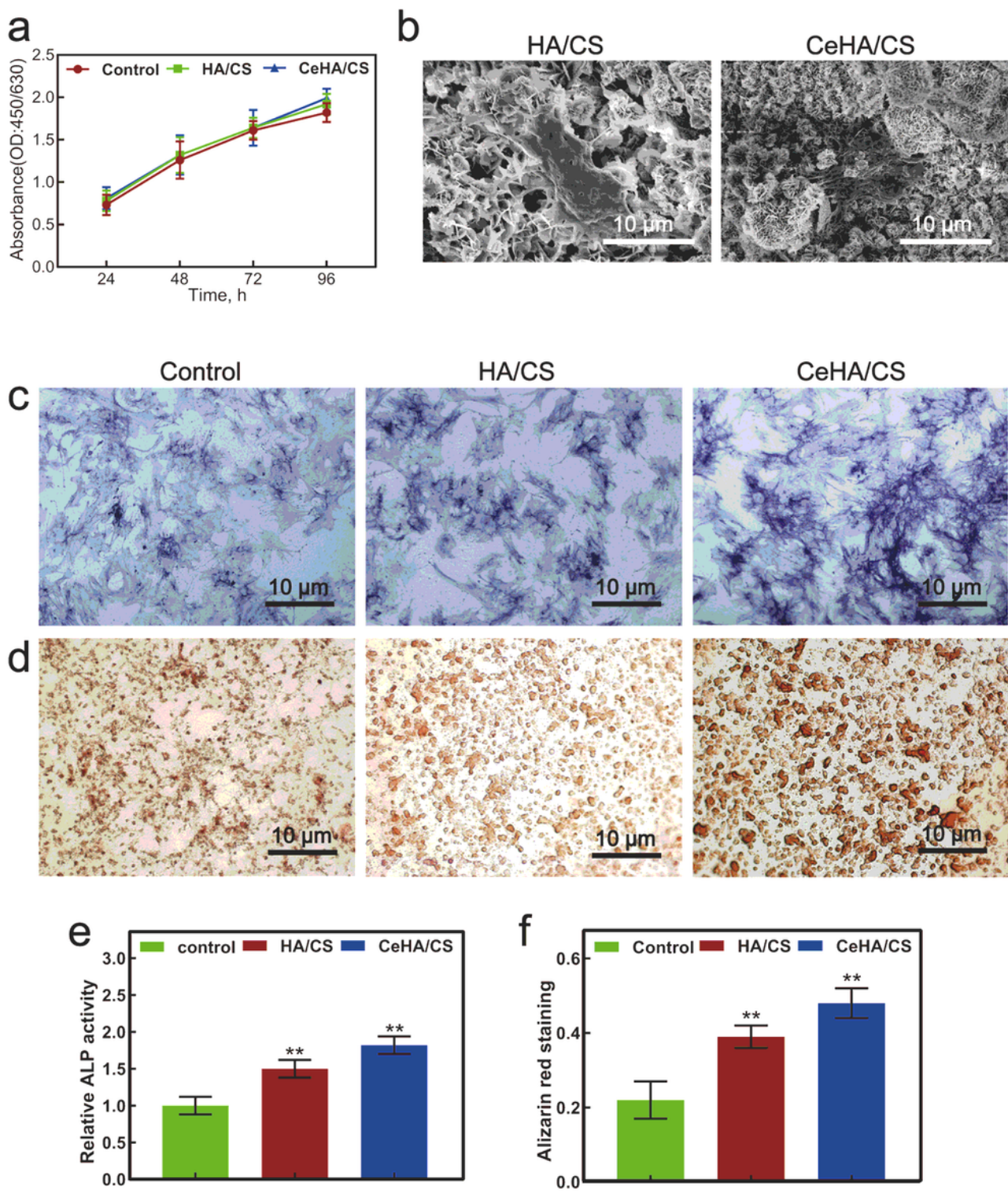


Figure 3

(a) CCK-8 analysis for control, HA/CS, and CeHA/CS scaffolds; (b) SEM images for HA/CS and CeHA/CS scaffolds; (c) ALP staining and (d) alizarin red staining images of hBMSCs cultivated with control, HA/CS and CeHA/CS scaffolds; (e) Relative ALP and (f) alizarin red activities in control, HA/CS and CeHA/CS scaffolds.

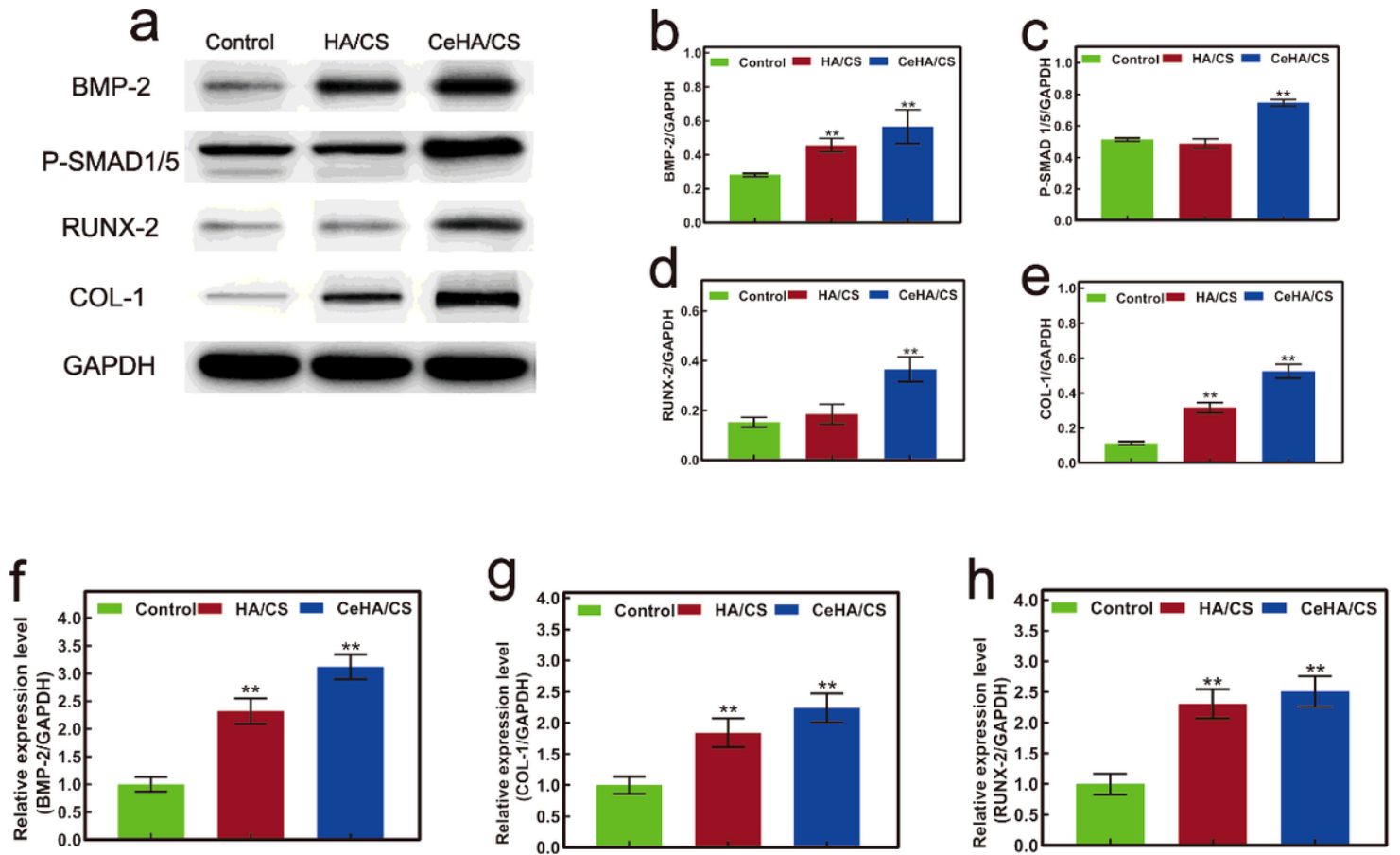


Figure 4

(a) Western-blot analysis for expressions of osteogenic genes in hBMSCs cultured with control medium, HA/CS and CeHA/CS scaffolds; (b) BMP-2, (c) P-SMAD 1/5, (d) RUNX-2, (e) COL-1 expressions in control, HA/CS and CeHA/CS scaffolds based on western blots; qPCR analysis of expressions levels of (f) BMP-2, (g) COL-1, (h) RUNX-2.

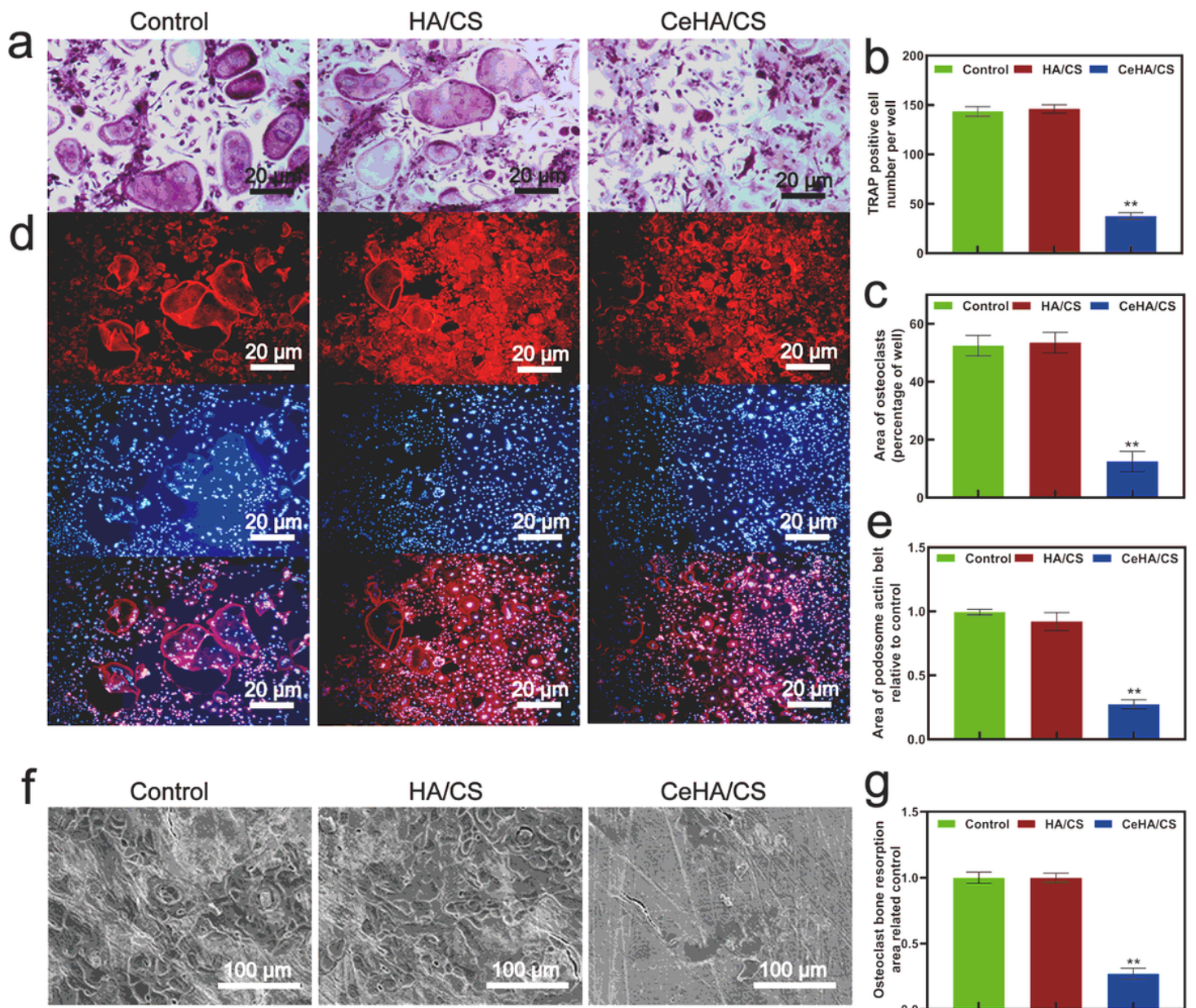


Figure 5

(a) TRAP staining in control, HA/CS and CeHA/CS scaffolds; (b) TRAP positive cell number per well; (c) Osteoclasts percentage area; (d) F-actin immunofluorescence staining of cells in control, HA/CS and CeHA/CS scaffolds. (e) Area of f-actin compared to control; (f) SEM images of bone resorption area; (g) Relative bone resorption area to control.

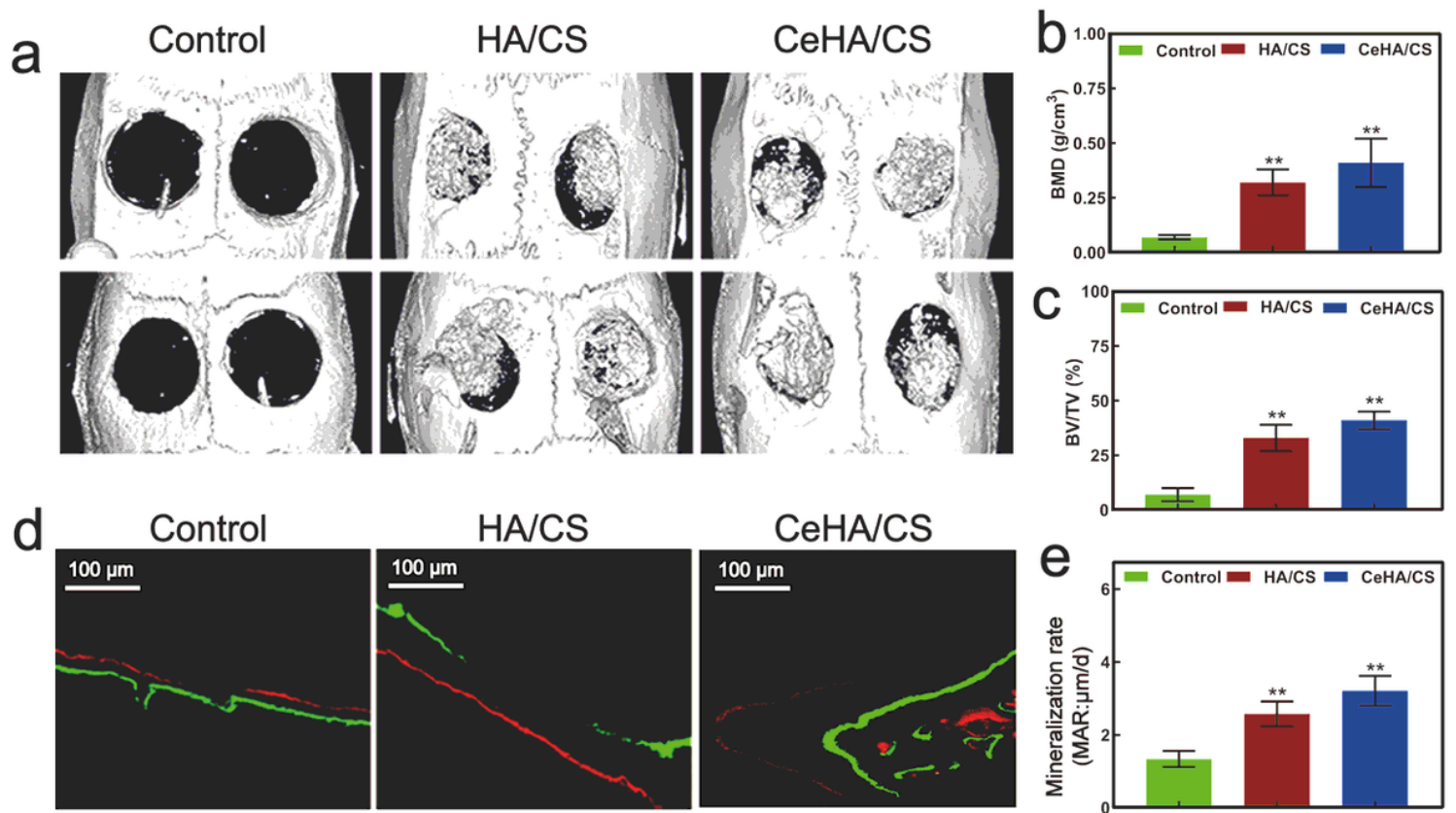


Figure 6

(a) Micro-CT imagines of rat calvarial defects in control, HA/CS and CeHA/CS scaffolds; (b) Bone mineral density; (c) Bone volume against tissue volume; (d) Fluorochromes marks of calcein (green) and alizarin red (red) 3 weeks and 3 days before euthanasia. (e) Mineralization rate.

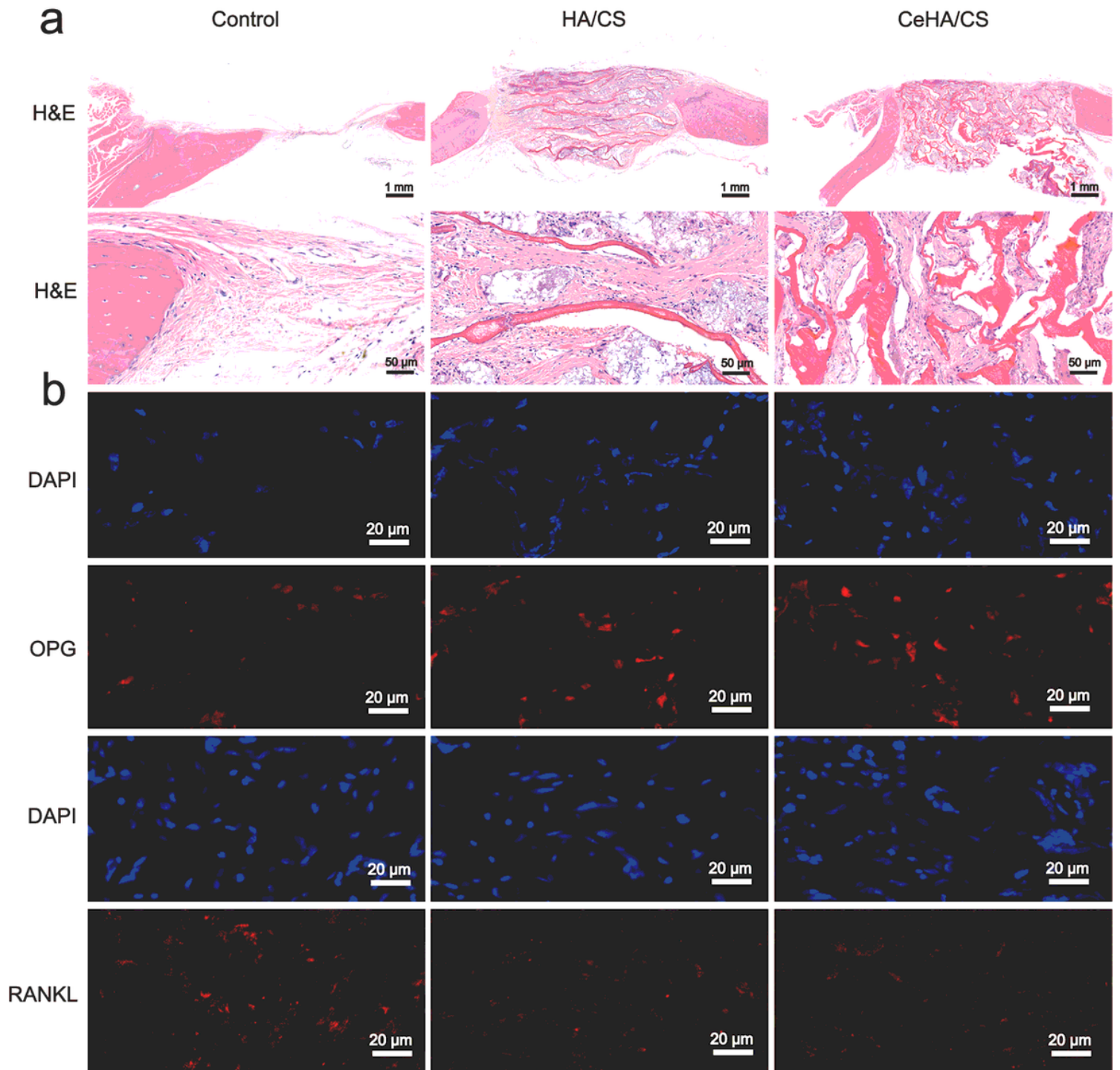


Figure 7

(a) H&E staining of the calvarial defect rats; (b) Immunofluorescence staining of DAPI, OPG and RANKL from the calvarial defect rats.